Check for updates

High-throughput computational workflow for ligand discovery in catalysis with the CSD†

Marc A. S. Short, [iD] [a] Clare A. Tovee, [iD] [c]
Charlotte E. Willans [iD] [b] and Bao N. Nguyen [iD] *[b]

A novel semi-automated, high-throughput computational workflow for ligand/catalyst discovery based on the Cambridge Structural Database is reported. Two potential transition states of the Ullmann–Goldberg reaction were identified and used as a template for a ligand search within the CSD, leading to >32 000 potential ligands. The $\Delta G^{\ddagger}$ for catalysts using these ligands were calculated using B97-3c//GFN2-xTB with high success rates and good correlation compared to DLPNO-CCSD(T)/def2-TZVPP. Furthermore, machine learning models were developed based on the generated data, leading to accurate predictions of $\Delta G^{\ddagger}$, with 70.6–81.5% of predictions falling within ± 4 kcal mol^{-1} of the calculated $\Delta G^{\ddagger}$, without the need for the costly calculation of the transition state. This accuracy of machine learning models was improved to 75.4–87.8% using descriptors derived from TPSS/def2-TZVP//GFN2-xTB calculations with a minimal increase in computational time. This new workflow offers significant advantages over currently used methods due to its faster speed and lower computational cost, coupled with excellent accuracy compared to higher-level methods.

1 Introduction

The development of organometallic catalysts, and suitable ligands, is a key challenge in the area of catalysis. While the process for traditional precious metals, such as Pd, Ru and Rh, is well established based on extensive mechanistic understanding and data-based approaches,[1–7] ligand design for base metal catalysts is still a nascent area of research and needs to balance many more catalytic and catalyst decomposition pathways.[8–10] Properties such as activity, selectivity and stability are the most common criteria when selecting a ligand, but solubility, toxicity and cost are also important properties to consider.[11] Recent applications of data science to catalysis have highlighted the computer-guided search for optimal ligands and reaction conditions as a major technology which can significantly progress this field of research.[12,13]

While high-throughput experimental approaches have proven effective at finding suitable ligands from libraries and optimising reaction conditions,[14–17] these are limited by the available ligand libraries. *In silico* ligand exploration allows faster access to the entire chemical space and can lead to the discovery of unexpected ligands. In addition, new developments in high-throughput computational techniques,[18–21] and cheminformatics tools can underpin additional filters such as ligand cost/complexity, toxicity and availability for a variety of applications in different chemical sectors.[22–24] However, research in this field has been hampered by a lack of suitable tools for the automated exploration of ligand space, while taking into account synthetic feasibility of the ligands.[13,25–27] In this paper, we report an alternative approach which leverages the extensive Cambridge Structural Database (CSD) and its tools to explore ligand space in a relevant catalytic reaction. This has the benefit of avoiding the synthetic feasibility challenge completely, while still maintaining a very wide chemical space coverage.

The approach was demonstrated with the copper(I)-catalysed Ullmann–Goldberg reaction, an important C–N cross-coupling reaction which has been highlighted by pharmaceutical companies as a desirable synthetic tool in the near future due to its mild conditions compared to the palladium-catalysed counterpart and sustainability credentials.[28] Despite this level of interest, the Pd-catalysed Buchwald–Hartwig coupling reaction is still preferred due to its reliability and better-developed ligands. Several different reaction mechanisms have been

[a] *School of Chemical and Process Engineering, University of Leeds, Woodhouse Lane, Leeds LS2 9JT, UK*

[b] *School of Chemistry, University of Leeds, Woodhouse Lane, Leeds LS2 9JT, UK. E-mail: b.nguyen@leeds.ac.uk*

[c] *The Cambridge Crystallographic Data Centre, 12 Union Road, Cambridge, CB2 1EZ, UK. E-mail: tovee@ccdc.cam.ac.uk*

† Electronic supplementary information (ESI) available. See DOI: https://doi.org/10.1039/d3cy00083d

This journal is © The Royal Society of Chemistry 2023

Catal. Sci. Technol., 2023, **13**, 2407–2420 | **2407**

proposed for this reaction, *e.g.* oxidative addition,[29,30] single electron transfer (SET),[31,32] atom transfer,[31] sigma bond metathesis,[33] and π-complexation of Cu(ɪ) on ArX,[34,35] which can depend on the substrates and ligands.[36–39] The mechanisms are further complicated by reversible deactivation of the catalyst by reversible disproportionation of a Cu(ɪ) intermediate into deactivated species,[40–42] and involvement of the base in the reaction mechanism.[43] Thus, little understanding of ligand design, which can improve reaction yields, scope, catalyst loading and catalyst stability, has been reported. This reaction serves as an excellent case study for our automated ligand discovery approach using the CSD and high-throughput calculation of activation energy barriers (Fig. 2). Two transition states, oxidative addition (**TSOA**) and sigma bond metathesis (**TSSig**), were chosen in this study. The other possible mechanisms, which require an accurate description of either open-shell complexes or weak interactions, were excluded due to the high computational cost required in a high-throughput context (Fig. 1).[44–47]
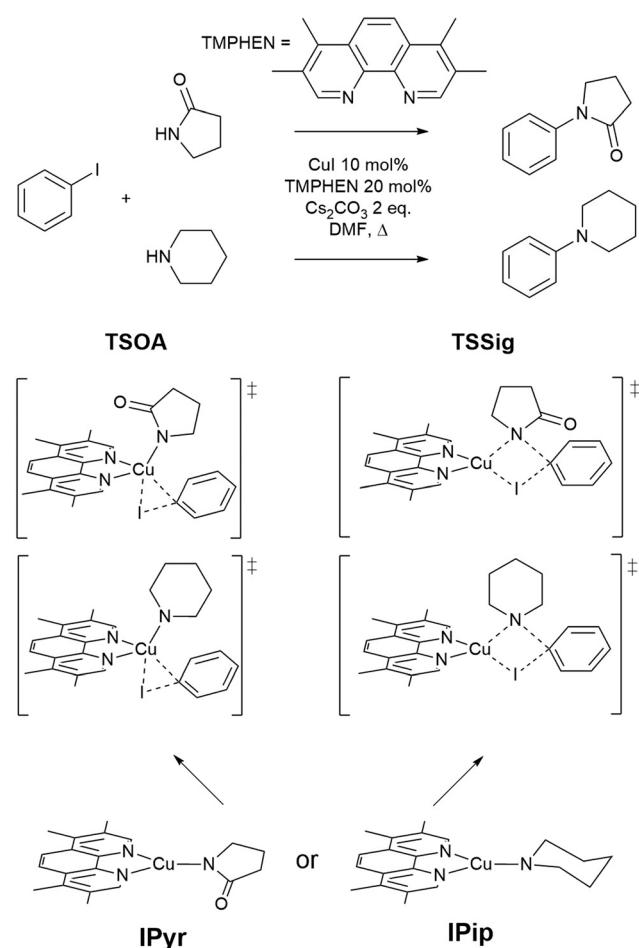
Fig. 1 The Ullmann–Goldberg coupling reactions studied and proposed transition states for oxidative addition (TSOA) and sigma bond metathesis (TSSig).

2 Methodology

2.1 Workflow for high-throughput catalyst design with the CSD

The workflow for the process of ligand identification from the CSD to building catalytic intermediates and transition states, to the calculation of activation energy barriers and machine learning (ML) descriptors are summarised in Fig. 2. The process is automated with *Python*. All automation code is included in the repository linked at the end of this manuscript.

2.2 Curation of literature ligands

Ligands were extracted from the Reaxys database for the C–N, C–O and C–S intermolecular Ullmann–Goldberg coupling, where the aryl halide is an aryl or heteroaryl chloride, bromide or iodide. For C–N coupling reactions, cyclic and acyclic amines and amides coupling partners were retrieved. Approximately 20 000 reactions were identified. Ligands contained in precatalysts were extracted manually. Reactions with no identifiable ligand (*e.g.* copper nanoparticles) and no reported yield were removed resulting in a total of 10 738, 2814, 750 entries for C–N, C–O and C–S coupling, respectively. From these entries, 345 unique ligands were identified. Structures of ligands were retrieved as a SMILES string using the Chemical Identifier Resolver (CIRpy).[48] Where no structure was found, the structure was retrieved manually. Where structures contain multiple components, *e.g.* tetrabutylphosphonium acetate, the counterion or solvent was removed using the Openbabel *Python* toolkit. These ligands form the ***ligands_lit_set***.

2.3 Ligands identification from the CSD

The CCDC CrossMiner tool was used to search the CSD for a *catalophore*, a 3D structural query made up of feature points describing the structural properties of the ligand and the desired transition state. These searches were performed on CSD_541 with the Mar20, May20, Aug20 and Feb21 updates. The following filters on structures were applied, leaving approximately 658 000 structures: (a) are not polymeric, (b) have no disorder, (c) for which 3D coordinates have been determined and (d) have a maximum *R*-factor of 10%. A new set of features were created for catalysis to enable searching of the CSD for common coordinating functional groups, defined using SMARTS strings, in organometallic chemistry. The new database is named ***CatSD***.

2.4 Building of complexes and transition states

A modified version of the *molSimplify Python* toolkit, which includes the additional ability for core-constrained force field optimisation, was employed to generate all structures.[49] Ligands and substrates are supplied as either a SMILES string or an *.xyz* or *.mol* 3D structure file. Deprotonation of ligand functional groups upon coordination to the metal (*i.e.* OH and 1,3-dione) is achieved through functional group

2408 | *Catal. Sci. Technol.*, 2023, **13**, 2407–2420

This journal is © The Royal Society of Chemistry 2023
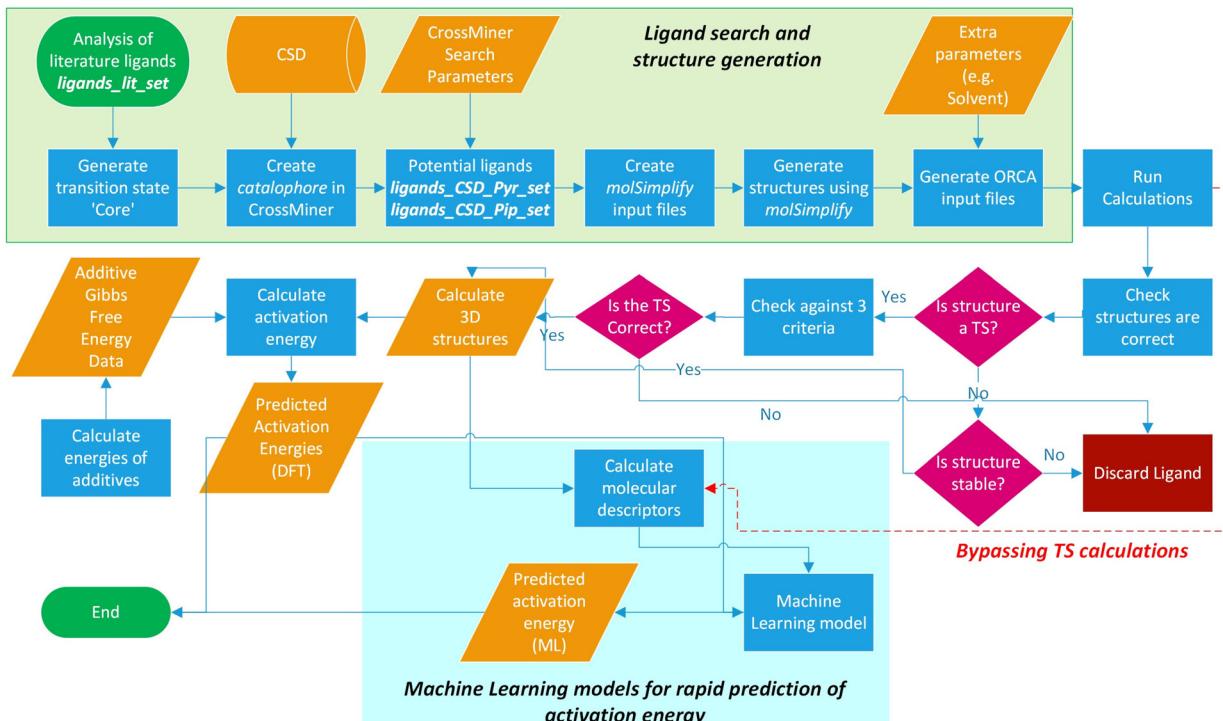
Fig. 2 Workflow overview for identifying ligands in the CSD, high-throughput calculation of $\Delta G^{\ddagger}$, and ML prediction of $\Delta G^{\ddagger}$ for *in silico* screening of catalysts.

matching, using a set of deprotonation rules generated from the analysis of protonation states of similar Cu(ɪ) complexes in the CSD (see ESI† Tables S2 and S3).

Catalytic intermediates **IPip** and **IPyr** (Fig. 1) are generated through standard complex generation with piperidine and 2-pyrrolidinone as coupling partners, in a singlet spin state. The structures are optimised before and after ligand addition using the Universal Force Field (UFF).[50] Transition state structures are generated *via* ligand replacement of a transition state template (**TSOA** or **TSSig**), generated with GFN2-xTB, using 3,4,7,8-tetramethyl-1,10-phenanthroline (TMPHEN) as the ligand, and iodobenzene as the aryl halide coupling partner. TMPHEN is then replaced using the ligand replacement feature included in *molSimplify* by defining the coordinating atoms of the new ligand(s). The structure is subsequently optimised with a custom after-core constrained method with UFF, where the transition state 'core' is locked and only the ligand(s) are optimised.

2.5 Molecular modelling

Benchmarking DFT calculations were performed in the gas phase using Gaussian09 Rev D.01.[51] xTB, B97-3c and coupled cluster calculations were performed in ORCA 4.2.1 interfaced with xtb 6.3.3.[19,52] ML DFT descriptor calculations use ORCA 5.0.1. Coupled cluster calculations were performed with the DLPNO-CCSD(T)/def2-TZVPP method.[53] All DFT methods use the SMD solvent model with DMF as the solvent.[54] GFN2-xTB methods use the generalised Born model with surface area

contributions (GBSA) solvent model for DMF.[55] Numerical Hessian were computed to determine the nature of the stationary points (zero and one for minima and transition states respectively) and to calculate the vibrational corrections at 298.15 K.

For B97-3c//GFN2-xTB high-throughput calculations, the structures were first optimised and numerical frequencies were calculated with GFN2-xTB. Energy calculations were performed at the B97-3c level of theory using DMF as the solvent.

For transition state vetting, the eigenvector corresponding to the imaginary frequency should have motion along one of the transition state active bond stretching modes, with an overlap above the threshold $S_0 = 0.20$ and 0.33 (eqn (2)) for **TSOA** and **TSSig**, respectively.

2.6 Energy and descriptor extraction

Gibbs free energies of simple reaction components, *e.g.* the base, counterions, and substrates, are calculated using standard protocols in DMF.

Descriptors for ML were chosen to describe steric and electronic properties of the respective complexes and transition states. All electronic descriptors were extracted from the B97-3c energy files, except the imaginary frequency which is from the GFN2-xTB frequency calculation. Electronic descriptors: HOMO energy, LUMO energy, Lowdin charge, bonded valence, atomic population, bond order and orbital charges. Bond descriptors are for all transition state active

This journal is © The Royal Society of Chemistry 2023

Catal. Sci. Technol., 2023, **13**, 2407–2420 | **2409**

bonds and Cu–L bonds. Electronic descriptors for individual atoms are for transition state active atoms and the ligand coordinating atoms, L1 and L2. Steric descriptors: bite angle, change in bite angle, cone angle, sterimol B1, B5, L, % buried volume at 3.5 Å, 5 Å and 7 Å, solvent accessible surface area, Cu–L bond lengths, bond angles and change in bond lengths between the transition state and CuLX starting structure, transition state active bond lengths and bond angles. Cu–L and transition state active steric descriptors were calculated directly from bond lengths and bond angles from the *.xyz* files. All other steric descriptors were calculated using the Morfeus *Python* package.[56]

2.7 Machine learning

Eight ML algorithms were employed; multiple linear regression (MLR), Gaussian process regression (GP), artificial neural networks (ANN), support vector machine (SVM), partial least squares (PLS), random forest (RF), extra trees (ET) and bagging (Bag). Default hyperparameters were tuned with the following exceptions: for GP only the Matern, radial basis function (RBF) and rational quadratic kernel were tuned; for ANN, n_odes (number of nodes in the hidden layers) was optimised with the number of hidden layers varied for SVM the RBF kernel was used with C, epsilon and gamma being optimised for PLS, n_components (number of components to retain after dimension reduction) was optimised and for RF, ET and bag, n_estimators (number of trees) and max_depth was optimised. These were optimised using the Optuna Python package, with performance metrics obtained using 10-fold cross-validation.[57] ML was performed in Python 3 with the scikit-learn module. Prior to ML, all

descriptors were scaled using a standard scaler. Models were set to optimise to a maximum for the coefficient of determination (R^2). For the evaluation of prediction models for $\Delta G^{\ddagger}$, datasets were split into training and test sets by binning the data in intervals of 1 kcal mol^{-1}. A proportional amount of data was taken from each bin to form a training set (~80% of the data) and a test set (~20% of the data). Each model was trained on the same training set and tested on the same unseen test set.

3 Results and discussion

3.1 Analysis of literature ligands and potential ligands in CSD

Analysis of literature Ullmann–Goldberg reactions contained within Reaxys resulted in 10728 C–N coupling reactions and 2814 C–O coupling reactions. From these, 345 literature ligands (281 bidentate and 64 monodentate) were extracted as the ***ligands_lit_set***. The majority of bidentate ligands are N–N, O–O or N–O ligands, with only 7% containing a donating sulfur or phosphorus group. Importantly, 67% of the bidentate ligand contain a 2-atom bridge, 26% a 3-atom bridge, and 3% a 4-atom bridge (see ESI,† Tables S4 and S5). Given the dominance of bidentate ligands with a 2-atom bridge, they were selected as the preferred mode of coordination for the ligand search. A ligand with a 2-atom bridge and second-row donor atoms (N, O), *i.e.* TMPHEN, was selected for generating the template structure for each transition state which would be employed in the ligand search (Fig. 3).

For these transition states, piperidine and 2-pyrrolidinone were selected as coupling partners in order to minimise
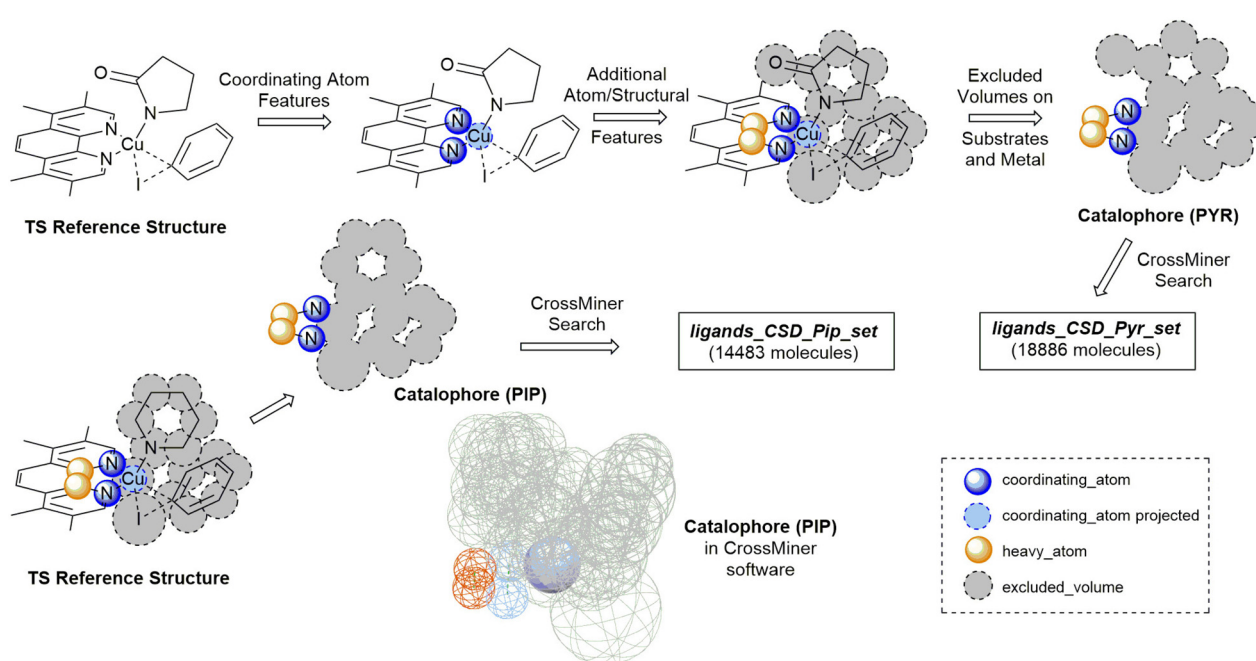

Fig. 3 Workflow for generation of a catalophore from a transition state reference structure and identification ligands in the CSD to generate ligand sets ligands_CSD_Pip_set and ligands_CSD_Pyr_set. Hydrogens are excluded for clarity.

2410 | *Catal. Sci. Technol.*, 2023, **13**, 2407–2420

This journal is © The Royal Society of Chemistry 2023

conformational flexibility in the organometallic intermediates and transition states (Fig. 1). In each case, a transition state was generated using GFN2-xTB using TMPHEN as the ligand, and iodobenzene as the aryl halide. The structure was optimised to a transition state and the imaginary frequency was checked for the correct vibrational mode (Fig. 3). These transition states were used as a reference structure for ligand identification in the CSD.

The **TSOA** structure with TMPHEN as the ligand was imported into CSD-CrossMiner and *coordinating_atom* features were placed on each TMPHEN nitrogen atom and projected onto the copper atom. A bridge of two *heavy_atom* features between the two coordinating nitrogens was placed on the two bridging carbon atoms. The tolerance for each atom was set at 0.75 Å after manual tuning. The features were constrained to be intramolecular. The substrate sites were defined by placing excluded volume features on each atom of the substrates with a tolerance equal to the van der Waals radii of the base atom. Thus, the created pocket represents the space occupied by both substrates in the transition state, with a soft tolerance allowing the vdW radii of atoms to overlap with the excluded cavity, to allow for variations in individual transition states with different ligands and substrates. Ligands which pre-arrange in this manner will more likely favour the required geometry of the transition state. Only organic structures were included in the search by setting *is_organic* to True. The catalophore was saved as a *.cm* file.

The *catalophore* searches were conducted using the CatSD structural database, a carefully curated subset of the CSD, with the CSD-PythonAPI. The searches were conducted with a maximum molecular weight of 500 Da, a maximum root-mean-square-deviation (RMSD) in geometry between catalophore and the hit of 1,[58,59] with Br, Cl, I, Li, Na, K, Ca, Mg, Be and transition metals excluded. SMILES code matching was used to remove duplicate structures. 3D structures were cleaned by assigning all unknown bond types, adding all missing hydrogens and setting all formal charges. Structures were exported in *.mol* format. In order to generate organometallic complexes with the ligands, the indexes of the coordinating atoms in the 3D structure file are required to define the bonds between the ligand and the metal centre. These were automatically identified for each ligand by matching the coordinates of the *coordinating_atom* features to the atoms located at those coordinates in the hit structure. The atom indexes, name of the structure file and charge of the ligand are exported as a *molSimplify .dict* file. This *.dict* file is used by *molSimplify* to obtain the data required for structure generation for each ligand.

For piperidine and 2-pyrrolidinone coupling partners, 14 483 (*ligands_CSD_Pip_set*) and 18 886 (*ligands_CSD_Pyr_set*) unique structures were identified as potential ligands in the CSD, respectively.

3.2 Choice of computational methods

As very high-throughput computational studies of organometallic complexes and transition states is a

relatively new area of research, there is no current consensus on the best methods for a given catalytic reaction. Thus, we decided to benchmark a wide range of semi-empirical and DFT methods (using the same basis set, def2-TZVP) for geometries of Cu(I) complexes and energies of transition states. All benchmarking complexes were taken from the CSD which contain the following: i) a mononuclear three-coordinate copper(I) centre, ii) a deprotonated N-ligand, iii) either one bidentate or two monodentate ligand(s). This led to a **Cu_benchmark_set** of 10 complexes with well-characterised structures (Fig. 4). The quality of the optimised structures is assessed on the basis of the reproduction of the coordination environment consisting of the metal–ligand bond lengths (d(Cu–L) in Å) and ligand–metal–ligand bond angles (∠(L–Cu–L) in °). The results are reported as the mean absolute error (MAE) against experimental values and are summarised in Table 1.
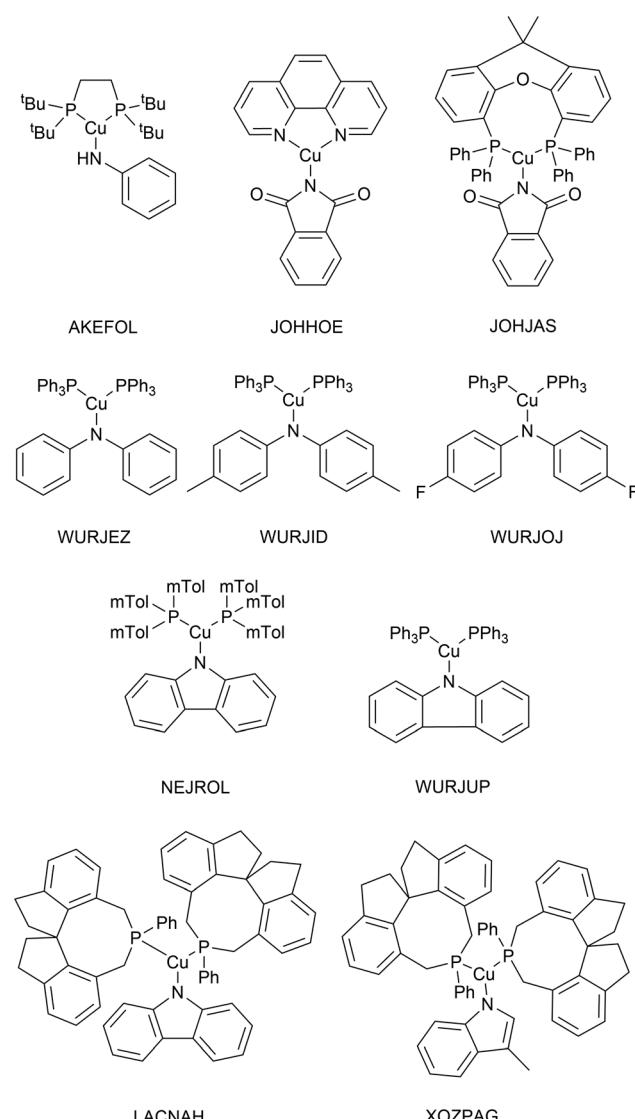

Fig. 4 Structures of the 10 Cu(I) complexes in the *Cu_benchmark_set*.

This journal is © The Royal Society of Chemistry 2023

Catal. Sci. Technol., 2023, **13**, 2407–2420 | **2411**

Without D3 dispersion correction, all methods overestimated bond lengths by several picometers due to the inability of the methods to account for London dispersion interactions and increased steric interactions at the metal centres. The GGA/meta-GGA functionals, BP86 and M06-L, perform better than the hybrid functionals when predicting bond lengths, with BP86 being the most computationally efficient (entry 9 and 12, Table 1). The inclusion of D3 dispersion correction led to significantly improved performance in all DFT methods. TPSSh, a meta-GGA hybrid including 10% HF exchange, showed the best predictions for both bond lengths and bond angles while keeping the computational cost relatively low. Importantly, GFN2-xTB calculations using xtb 6.3.0 with *verytight* optimisation criteria showed excellent structural agreement with the crystal structures with minimal computational cost (entry 3, Table 1). The composite method B97-3c gave even better results (MAE of 0.013 Å and 2.3°), requiring only 84 hours of single-core CPU time, compared to 6172 hours for TPSSh-D3(BJ) and 4036 hours for BP86-D3(BJ). In fact, B97-3c outperformed the best DFT functional TPSSh-D3(BJ), even with a full triple-ζ basis set. Thus, the GFN2-xTB and B97-3c methods are the most suitable computational methods for very high-throughput computational studies of the Ullmann–Goldberg reaction (Fig. 5).

Lastly, the accuracy of the high-throughput calculation of $\Delta G^{\ddagger}$ for the Ullmann–Goldberg reaction was assessed. Grimme and co-workers have demonstrated that the B97-3c// GFN2-xTB combination can be as accurate as traditional DFT methods in optimising and calculating energy-related properties of stable organometallic compounds.[21,60] However,

its performance in calculating transition states is unknown. Thus, we benchmarked the accuracy of B97-3c//GFN2-xTB calculated $\Delta G^{\ddagger}$ values (B97-3c single point energy with GFN2-xTB vibrational correction) against those obtained by the 'gold standard' method for the calculation of structure energies, CCSD(T), for 100 randomly selected literature ligands. Both energy calculations used the same GFN2-xTB optimised structures. Coupled cluster energies were calculated at the DLPNO-CCSD(T)/def2-TZVPP level of theory and compared to the B97-3c energy. The results are summarised in Fig. 6.

The activation energies barriers calculated by B97-3c were found to correlate reasonably well with those obtained with DLPNO-CCSD(T)/def2-TZVPP method ($R^2 = 0.5774$ for a linear relationship $y = 0.8938x + 8.3679$). Therefore, the B97-3c derived values were scaled (see ESI,† section 2.2), achieving a mean average error (MAE) of 3.9 kcal mol^{-1} (Fig. 6). The majority of calculated $\Delta G^{\ddagger}$ (89%) fell with 15× RMSE of the benchmarked values. Thus, the B97-3c method represents a good balance between computational time and accuracy for the calculation of activation energies of Ullmann–Goldberg reactions. Structures containing oximes and O–Cu–O 5-membered ring motifs correlate poorly between the two methods. However, only 8 ligands containing oximes have been reported for the Ullmann–Goldberg reaction (*ligands_lit_set*), and this was not deemed a significant problem for ligand exploration.

Based on the benchmarking results all optimisations and frequency calculations were performed using GFN2-xTB. Energy calculations were carried out using the B97-3c composite method.

3.3 High-throughput calculation of $\Delta G^{\ddagger}$

Once the potential ligands were identified, all corresponding structures of catalytic intermediates and **TSOA** and **TSSig** transition states for each of the ligands were generated using a modified version of *molSimplify*.[49] There are two key challenges in automating this process: (i) determining the coordination sites in ligands with more than 2 feasible sites (*ligands_lit_set* only); and (ii) determining whether

Table 1 Assessment of electronic structure methods and density functionals with the def2-TZVP basis set, in terms of the mean absolute error in metal–ligand bond length (Cu–L, Å), ligand–metal–ligand bond angle (L–Cu–L, °) and single-core computational time (Intel Xeon Gold 6138 CPU @ 2.0GHz, 1GB RAM per core) for *Cu_benchmark_set*

| Entry | Method/functional | MAE | | Time (h) |
		d(C–uL) (Å)	∠(L–Cu–L) (°)	
1	GFN0-xTB	0.149	13.2	0.9
2	GFN1-xTB	0.073	4.6	2.0
3	GFN2-xTB	0.029	4.7	1.7
4	HF-3c	0.287	29.0	145
5	PBEh-3c	0.035	3.3	503
6	B97-3c	0.013	2.3	84
7	B3LYP	0.066	4.2	4931
8	M06	0.034	3.4	7850
9	M06-L	0.020	4.1	7127
10	TPSSh	0.032	3.9	5435
11	MPWLYP1M	0.063	4.3	6508
12	BP86	0.030	4.2	2143
13	wB97xD	0.030	4.3	9220
14	B3LYP-D3(BJ)	0.023	3.7	6179
15	M06-D3(0)	0.028	3.5	11 140
16	M06-L-D3(0)	0.019	4.3	5271
17	TPSSh-D3(BJ)	0.016	3.3	6172
18	TPSS-D3(BJ)	0.017	3.7	3886
19	PBE0-D3(BJ)	0.018	3.6	5502
20	BP86-D3(BJ)	0.026	4.6	4036
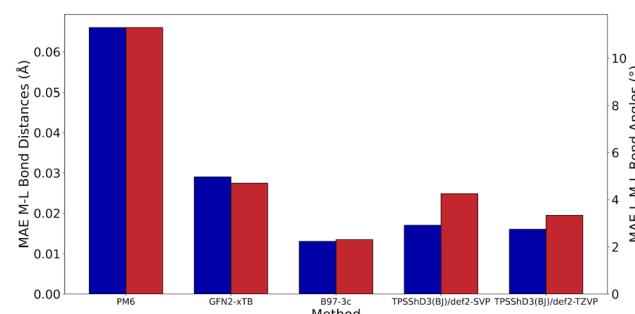
Fig. 5 Geometrical benchmarking results for the best-performing methods in each class (semi-empirical, extended tight binding, 3c and DFT), mean absolute error in metal–ligand bond length (blue) and ligand–metal–ligand bond angle (red), for the *Cu_benchmark_set*.

2412 | *Catal. Sci. Technol.*, 2023, **13**, 2407–2420

This journal is © The Royal Society of Chemistry 2023
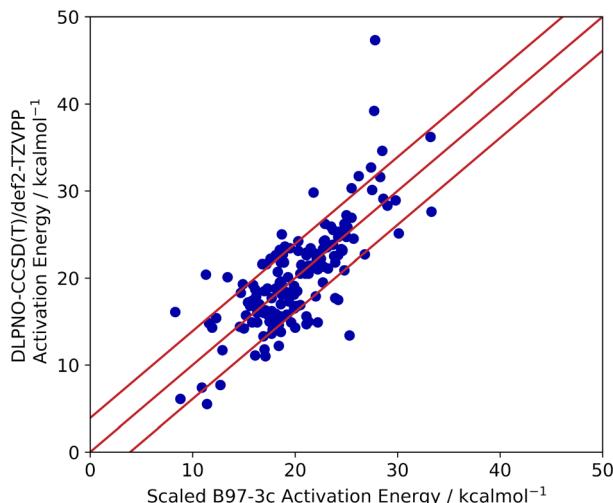
Fig. 6 Scaled B97-3c activation energies of 68 TSOA and 83 TSSig transition states from *ligands_lit_set*, compared to their DLPNO-CCSD(T)/def2-TZVPP calculated activation energies. The red lines represent 3.9 kcal mol^{-1} (the MAE in the calculations).

deprotonation of any coordination site is required prior to coordinating to Cu(ı). The first challenge was addressed *via* a combinatory approach, generating all possible bidentate combinations between the ligand and Cu(ı) cation. The second challenge was addressed *via* analysis of Cu(ı) complexes of similar ligands. For this, the CSD was searched for Cu(ı) complexes with each functional group (*e.g.* alcohol, amine) both with and without the presence of a proton (*e.g.* OH–Cu and O–Cu). The number of search results for each indicated whether the functional group should be protonated or deprotonated during complex generation (see ESI,† Tables S2 and S3). Generally, functional groups with a pK_a < 25 (DMSO) were deprotonated upon coordination.

Conversion of ligands into complexes using SMARTS/ SMILES strings and *rdkit* package can suffer from conformational variation from those in the CSD. Thus, ligands are taken as *.xyz* or *.mol* 3D structure files derived from their structures in the CSD. For *ligands_lit_set*, SMILES strings were used due to the lack of suitable 3D structures in the CSD, and monodentate ligands were excluded for simplicity.

In order to automate the generation of transition states **TSOA** and **TSSig**, a different strategy was employed. The transition states generated with TMPHEN above were employed as templates and TMPHEN was substituted with the ligand of interest. These structures were then pre-optimised with a custom after-core constrained method using the universal force field (UFF), where the transition state 'core' is locked and only the ligand is optimised to ensure the transition state mode is preserved.

The structures generated by *molSimplify* were pre-optimised with GFN2-xTB with the *TightOpt* optimisation criteria with the transition state active atoms frozen. The resulting structure was considered close to the transition state and was then optimised using eigenvector following to

the transition state. To ensure reliability in cases with a shallow PES the exact Hessian is calculated every five optimisation steps. The presence of a transition state is verified by the presence of a single imaginary frequency. Single point energies are calculated with B97-3c using the *TightSCF* criteria and *SlowConv* to improve the reliability of SCF convergence. It is worth noting that many potential energy surfaces for **TSOA** and **TSSig** are relatively flat, requiring frequency Hessian calculations which are more costly computationally.

Preliminary examination of automated results showed that the process is prone to generating wrong transition states, *e.g.* a methyl rotation, dissociation of reactants, no identified transition state and hydrogen transfer between the ligand and the amine/amide. In order to validate the computed transition states, the vetting criteria presented by Jacobsen *et al.* were used.[61] This procedure is not based on an IRC calculation and, therefore, reduces the required computational time. The transition state structure must meet the following three criteria: i) exactly one imaginary frequency of the Hessian (a cutoff value of −40 cm^{-1} is used to remove structures with frequencies that could be considered as numerical noise); ii) the transition state active bonds (bonds being broken or formed) must be of an intermediate length (eqn (1)),

$$1.7 \geq \frac{r_{ij}}{\left(r_i^{\text{cov}} + r_j^{\text{cov}}\right)} > 1.0 \qquad (1)$$

where r_{ij} is the bond length between atoms i and j and r_i^{cov} and r_j^{cov} are the covalent radii of atoms i and j; iii) the eigenvector corresponding to the imaginary frequency should have motion along the transition state active bond stretching mode (eqn (2)),

$$|v_i^{\text{stretch}} \cdot v^{\text{ts}}| \geq S_0 \qquad (2)$$

where v^{ts} is the eigenvector of the imaginary frequency, v_i^{stretch} is the unit vector of the stretching mode of bond i and S_0 is a constant of default value 0.33. The value of S_0 needs to be tuned for different types of transition states.[61]

To assess the accuracy of the workflow in generating and optimising the transition states, 198 ligands from *ligands_CSD_Pip_set* were used as test cases. Both oxidative addition (**TSOA**) and sigma metathesis (**TSSig**) transition states with piperidine as the N-partner were generated and optimised. Manual inspection of the structures and visualisation of the imaginary frequency of a subset of ligands gave an optimal value of S_0 = 0.20 and 0.33 for **TSOA** and **TSSig** respectively, for the Ullmann–Goldberg reaction. For intermediates CuLI and **IPip**, 98% of all structures containing bidentate ligands were successfully generated (Table 2). For optimisation, 80% of CuLI and 56% of **IPip** structures were correctly optimised in an automated manner. Compared to these, the optimisation of transition states was very successful, giving a success rate of 63% for **TSOA** and

88% for **TSSig**. The most common reason for optimisation failure is low imaginary vibrational frequencies (>-20 cm^{-1}). This is likely due to poor starting structures generated from SMILES strings. To mitigate this on the CSD datasets, all structures (ligands and nucleophiles) were supplied as either X-ray or optimised 3D structures and the *TightOpt* criteria was used to aid the removal of small imaginary frequencies.

When this workflow was applied to the entire **ligands_CSD_Pip_set** and **ligands_CSD_Pyr_set**, the optimisation success rates for stable intermediates were significantly higher than those for **ligands_lit_set**, thanks to the initial 3D ligand structures supplied from the CSD. On the other hand, the success rates for transition states are significantly lower than those of **ligands_lit_set**. The success rate of finding and optimising **TSOA** (33%) was particularly low using **ligands_CSD_Pip_set** (Table 2). This result reflects that many potential ligands are not suitable for the Ullmann–Goldberg coupling reaction, as suggested by the experimental literature. **TSSig** is less sterically demanding than **TSOA** and consequently resulted in better success rates with both ligand sets. Similarly, as 2-pyrrolidinone is less sterically demanding than piperidine, the success rate in optimising **TSOA** is significantly higher with **ligands_CSD_Pyr_set** comparing to that with **ligands_CSD_Pip_set**.

The real-world runtime on a high-performance computing system using 4 cores and 4GB of RAM per job for **ligands_CSD_Pip_set** is ~6 weeks for 14 483 ligands. The comparative time for **ligands_CSD_Pyr_set** is ~4 weeks for 18 886 ligands after fine-tuning.

3.4 Factors influencing $\Delta G^{\ddagger}$ of the Ullmann–Goldberg reaction

Previous computational studies on Pd-catalysed reactions have shown the dependence of $\Delta G^{\ddagger}$ on the electronic properties of the ligand and its bite angle.[62,63] Understanding similar relationships in Cu(ı)-catalysed coupling reactions is an important milestone in ligand design for these catalysts. Thus, an analysis of the properties of the calculated transition states and their relationship to the calculated $\Delta G^{\ddagger}$ was performed. These properties were selected to represent the steric and electronic properties of the catalytic centre in the TS, which should influence its stability and the calculated $\Delta G^{\ddagger}$. A full table of properties/descriptors is available in the ESI† (section 5.4.4). Particular attention was given to the steric descriptors, given the shorter Cu–C/N/O bonds compared to those of palladium. Surprisingly, no clear

relationship with individual descriptors was observed with any of the four sets of calculated transition states(***Pyr_set_TSOA***, ***Pyr_set_TSSig***, ***Pip_set_TSOA***, and ***Pyr_set_TSSig***). All properties of both the TS and the starting intermediate have little to no impact on $\Delta G^{\ddagger}$ (see ESI† Table S11). This highlights the unique nature of Cu(ı) d^{10} catalytic centre, which is less sensitive to the ligand field and electronic properties of the ligand. The activation energy distributions for **ligands_CSD_PIP_set** are similar across both transition states with an average $\Delta G^{\ddagger}$ of ~18 kcal mol^{-1} (Fig. 7a). Closer examination showed the values for each ligand are generally close, with a small number of ligands giving very low or very high $\Delta G^{\ddagger}$ for **TSOA** with piperidine as the N-partner (Fig. 8). With 2-pyrrolidinone as the N-partner, there is a clear difference in $\Delta G^{\ddagger}$ between the **TSOA** (~18 kcal mol^{-1}) and **TSSig** (~38 kcal mol^{-1}) transition states. This suggests that for an amide nucleophile, the oxidative addition pathway is energetically more favourable than the sigma metathesis pathway. This difference in energy is likely due to the strain introduced to the amide bond, the N-atom changing from a trigonal planar to tetrahedral geometry, in the **TSSig** transition state. On the whole, **TSOA** is often either more favourable or as likely as **TSSig** in this type of Ullmann–Goldberg coupling reaction.

3.5 Predicting $\Delta G^{\ddagger}$ with machine learning

3.5.1 Descriptor selection. As no straightforward correlation was found between the calculated $\Delta G^{\ddagger}$ and the expected electronic and steric properties of the transition states of the Ullmann–Goldberg reaction, machine learning (ML) was leveraged to probe for more complex relationships between them. Regression models for $\Delta G^{\ddagger}$ based on the properties of **IPyr**, **IPip**, **TSOA** and **TSSig** may improve our understanding of factors which are important in designing ligands/catalysts for the Ullmann–Goldberg coupling reaction. Thus, a wide range of computational descriptors were generated based on these structures. For transition states, 14 steric and 11 electronic descriptors, for the ligand coordinating atoms L1 and L2, Cu and Cu and the TS active atoms (*i.e.* I, C and N) were generated from the B97-3c outputs. Similar descriptors were derived for **IPip** and **IPyr** as appropriate. The total numbers of descriptors for each dataset are summarised in Table 3 (see ESI,† Tables S9 and S11). Additional descriptors were included for **IPyr** and transition states with 2-pyrrolidinone, to account for the additional amide group (the C–N and C=O bonds, and

Table 2 Structure generation and optimisation (inside bracket) success rates for the high-throughput calculations for both nucleophiles

Structure	Ligands_lit_set^a	Ligands_CSD_Pip_set	Ligands_CSD_Pyr_set
CuLI	98 (80)	99 (85)	99 (84)
IPip/IPyr	98 (56)	99 (77)	99 (89)
TSOA	97 (63)	99 (33)	99 (61)
TSSig	99 (88)	99 (85)	99 (83)

^{a} Only bidentate ligands for piperidine.

2414 | *Catal. Sci. Technol.*, 2023, **13**, 2407–2420

This journal is © The Royal Society of Chemistry 2023
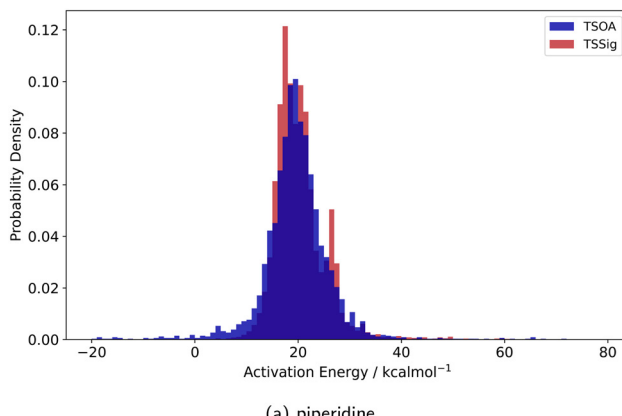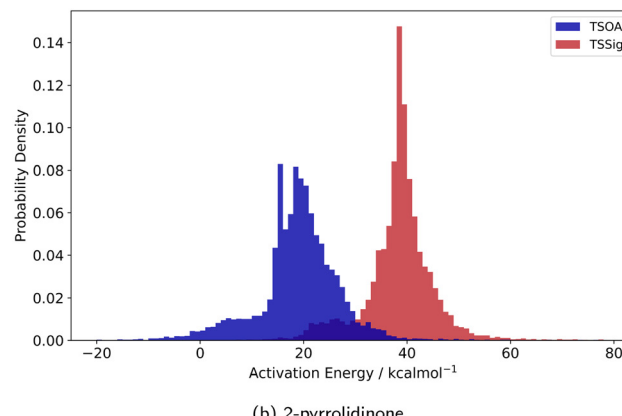
Fig. 7 Probability density for the activation energies of the **TSOA** (blue) and **TSSig** (red) transition states for piperidine (left) and 2-pyrrolidinone (right).

associated charges and molecular orbitals). In order to improve interpretability, the descriptors were trimmed by removing all but one highly correlated descriptor based on Pearson's coefficient (Table 3).

Common practice in ML relies on R^2 and RMSE, which do not consider the level of noise in training data, to evaluate models. Consequently, a new metric was created to evaluate the models: % of $\Delta G^{\ddagger}$ prediction within ± 4 kcal mol^{-1} (%$\Delta G^{\ddagger}$ ± 4). This reflects the maximum accuracy of the model based on the error present in the DFT calculated activation energies. Calculated datasets were trimmed *via* binning to remove bias from the uneven distribution of activation energies. Entries with a Cu–L bond order of 0 were discarded as they were bonding in a monodentate manner.

3.5.2 Prediction of $\Delta G^{\ddagger}$ with transition state derived descriptors. Eight ML algorithms: MLR, PLS, ANN, SVM, GP, RF, ET and Bag were applied to all 4 datasets (*Pip_set_TSOA*, *Pip_set_TSSig*, *Pyr_set_TSOA*, and *Pyr_set_TSSig*). Each dataset was randomly split into a training set (80% of the data) and test set (20%) by binning into 1 kcal mol^{-1} bins. Hyperparameters were optimised using the *Optuna* Python

module then evaluated. For all datasets, the ET algorithm gave the best metrics (Table 4) with the other tree-based algorithms (RF and Bag) and SVM giving comparable results. Linear algorithms (MLR and PLS), ANN and GP gave significantly poorer results (see ESI,† section 5.4.1). While 6678% of the predictions were within computational errors, RMSE across all datasets is significantly higher than expected DFT errors in calculating $\Delta G^{\ddagger}$ (3.9 kcal mol^{-1}). Prediction accuracy was generally good, with the majority of prediction within ±4 kcal mol^{-1} of the DFT calculated values. Predictions at <10 kcal mol^{-1} and >35 kcal mol^{-1} (>55 kcal mol^{-1} for PYR_set_TSSig) are generally poor with errors >8 kcal mol^{-1}. Manual examination of the outliers (>6 kcal mol^{-1}, 15× RMSE) showed that structures of the transition states for these outliers were incorrect. Several negative values were the result of H-bonding within the transition state, stabilising it compared to the intermediates **IPip** and **IPyr**. In most cases, they had incorrect ligand structures or formed strained 4-membered chelates (10–20 for each dataset). These were reliably identified as outliers with all algorithms, which unveiled a new method of rapidly screening failed transition state calculations. The outliers were removed from the datasets for subsequent models.
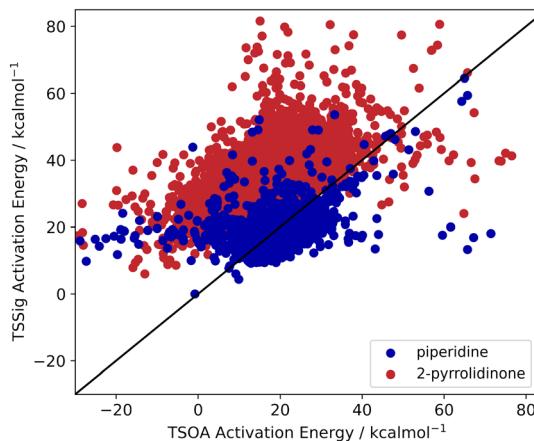
Fig. 8 **TSOA** activation energy against **TSSig** activation energy for piperidine (blue) and 2-pyrrolidinone (red).

Table 3 Number of descriptors at different stages in the descriptor trimming process

Dataset	Original	Highly correlated removed	Low importance removed
TS dependent			
PIP_set_TSOA	78	75	20
PYR_set_TSOA	128	111	24
PIP_set_TSSig	91	90	36
PYR_set_TSSig	130	121	41
TS independent			
PIP_set_TSOA_NoTS	67	60	10
PYR_set_TSOA_NoTS	67	62	14
PIP_set_TSSig_NoTS	67	61	27
PYR_set_TSSig_NoTS	67	62	17

This journal is © The Royal Society of Chemistry 2023

Catal. Sci. Technol., 2023, **13**, 2407–2420 | **2415**

Table 4 Metrics of the best-performing models with optimised hyperparameters for all four datasets with and without the optimised descriptor sets

Dataset	Best algorithm	R^2	RMSE	$\%\Delta G^{\ddagger} \pm 4$
Full descriptors				
PIP_set_TSOA	ET	0.49	7.90	75.5
PYR_set_TSOA	ET	0.65	6.32	66.1
PIP_set_TSSig	ET	0.39	5.93	77.9
PYR_set_TSSig	ET	0.63	5.52	68.5
Trimmed descriptors				
PIP_set_TSOA	ET	0.66	4.81	79.6
PYR_set_TSOA	ET	0.71	4.86	71.3
PIP_set_TSSig	ET	0.48	4.33	81.5
PYR_set_TSSig	ET	0.66	4.95	70.6

The importance of each descriptor was evaluated using permutation importance over 50 runs.[64] Those which showed a permutation importance of mean − 2 × std ≤ 0 (mean = average decrease in R^2 over 50 runs, std = standard deviation of the decrease in R^2 over 50 runs; this metric means that more than 95% of the permutation importance values from 50 runs are above 0) were removed. This led to a very significant reduction in the number of descriptors in each dataset (Table 3), improving the interpretability of the prediction models. Importantly, the removal of the redundant descriptors led to improvement in all metrics by a significant margin (Table 4).

3.5.3 Importance of ligand properties *via* permutation importance. Analysis of the 10 most important descriptors in each dataset (ET models) showed that **TSOA** $\Delta G^{\ddagger}$ strongly depends on orbital charges of the Cu s, d and I d orbitals and the HOMO energy (Table 5). This suggests that the ability

Table 5 The ten most important descriptors for each dataset based on permutation importance analysis of the ET models

Pip_set_TSOA	Pyr_set_TSOA
Orbital_charge_I_d	HOMO_energy
HOMO_energy	Orbital_charge_Cu_d
Orbital_charge_Cu_d	Orbital_charge_Cu_s
Lowdin_charge_C	Orbital_charge_L1_px
D_bite_angle	LUMO_energy
LUMO_energy	Orbital_charge_L2_px
Bond_order_Cu_L2	Atomic_population_L2
Lowdin_charge_Cu	D_bite_angle
Bonded_valence_I	Lowdin_charge_Cu
Orbital_charge_C_pz	Orbital_charge_Cu_p

Pip_set_TSSig	Pyr_set_TSSig
Atomic_population_Cu	HOMO_energy
Bite_angle	Atomic_population_Cu
Orbital_charge_N_s	N-Cu-I_angle
LUMO_energy	Atomic_population_amide_O
Orbital_charge_I_s	Atomic_population_N
C-N-Cu_angle	Orbital_charge_Cu_s
Orbital_charge_Cu_d	Bond_order_Cu-N
HOMO_energy	Cu-I-C_angle
Cu-L1_distance	Orbital_charge_amide_C_s
Cone_angle	Bond_order_Cu-I

Descriptors are colour coded: red for aryl halide, brown for Cu centre, cyan for the ligand, teal for the N-partner, and green for bond angles and bond lengths.

of the ligand to influence the electronic properties of the copper centre is an important factor in the activity of the ligand. $\Delta G^{\ddagger}$ for piperidine showed higher importance for descriptors localised on the aryl halide such as the bonded valence of the iodine atom and the charge on the aryl carbon atom, which are linked to the progress of the C–I bond cleavage at the transition state. With 2-pyrrolidinone as the N-partner, the charge on the copper s orbital and atomic population on the ligand coordinating atoms are important properties. The additional stabilisation of the negative charge on the amide nitrogen through the amide bond reduces the charge density of the copper centre and electron-donating ligands were found to promote **TSOA**.

For **TSSig**, $\Delta G^{\ddagger}$ showed high dependence on the atomic population on the Cu centre, Cu–N and Cu–I bond orders and TS mode bond angles, HOMO/LUMO energies and orbital charges of the Cu s, d, N s and I d orbitals. The sigma metathesis pathway showed strong dependence on steric descriptors (distances and angles). The amide C–O bond length and C–N bond order are important properties for coupling with 2-pyrrolidinone. This implies that the ability of the ligand to modulate the electron density of the copper centre to bond to and weaken the amide bond in the nucleophile is important. For piperidine, no such trend was observed, indicating a lesser degree of influence from the amine partner beyond a direct sigma donation to the Cu centre.

3.5.4 Prediction of $\Delta G^{\ddagger}$ without transition state derived descriptors. Using ML to predict $\Delta G^{\ddagger}$ clearly should avoid the actual DFT optimisation and energy calculation of the transition states themselves once the model is trained. The computational time required for the calculation of **TSOA** and **TSSig** accounted for 85–90% of the overall computational time required for both datasets (Table 6). A ML model which predicts $\Delta G^{\ddagger}$ without needing to calculate transition states will significantly speed up discovery workflows.

For this purpose, only descriptors based on **IPyr** and **IPip** were selected and subjected to the same descriptor trimming process (Table 3). Descriptors for individual atoms were extracted for Cu, N and ligand coordinating atoms (L1 and L2). For **ligands_CSD_PYR_set**, descriptors were also extracted for the amide C and O atoms. This resulted in four datasets, **PIP_set_TSOA_NoTS**, **PIP_set_TSSig_NoTS**, **PYR_set_TSOA_NoTS** and **PYR set_TSSig_NoTS** containing 67 descriptors and 1683, 3708, 3990 and 5798 ligands respectively (Fig. 9).

The results for the transition state independent models, using the same algorithms, are summarised in Table 7. Predictably, these new models show reduced accuracy compared to those with descriptors from the transition states, except for **PYR_set_TSOA_NoTS** which shows a slight improvement in R^2 (0.67 to 0.69) and RMSE (5.16 to 4.97). Nevertheless, the significant reduction of computational time (5.7–10 times) for new predictions with only a small decrease in accuracy was promising.

2416 | *Catal. Sci. Technol.*, 2023, **13**, 2407–2420

This journal is © The Royal Society of Chemistry 2023

Table 6 Breakdown of the single-core computational time for *ligands_CSD_PIP_set* and *ligands_CSD_PYR_set* datasets

Structure	Single-core computational time (h)			
	Optimisation	Energy + frequency	Total	% of time
Ligands_CSD_PIP_set				
CuLI	66	6244	6310	3.5
IPip	169	9897	10 067	5.6
TSOA	102 971	15 373	118 336	65.6
TSSig	30 829	14 957	45 787	25.4
Ligands_CSD_PYR_set				
CuLI	1173	8596	9789	6.0
IPyr	1693	11 618	13 312	8.2
TSOA	69 212	17 949	87 162	53.6
TSSig	33 253	19 212	52 466	32.2
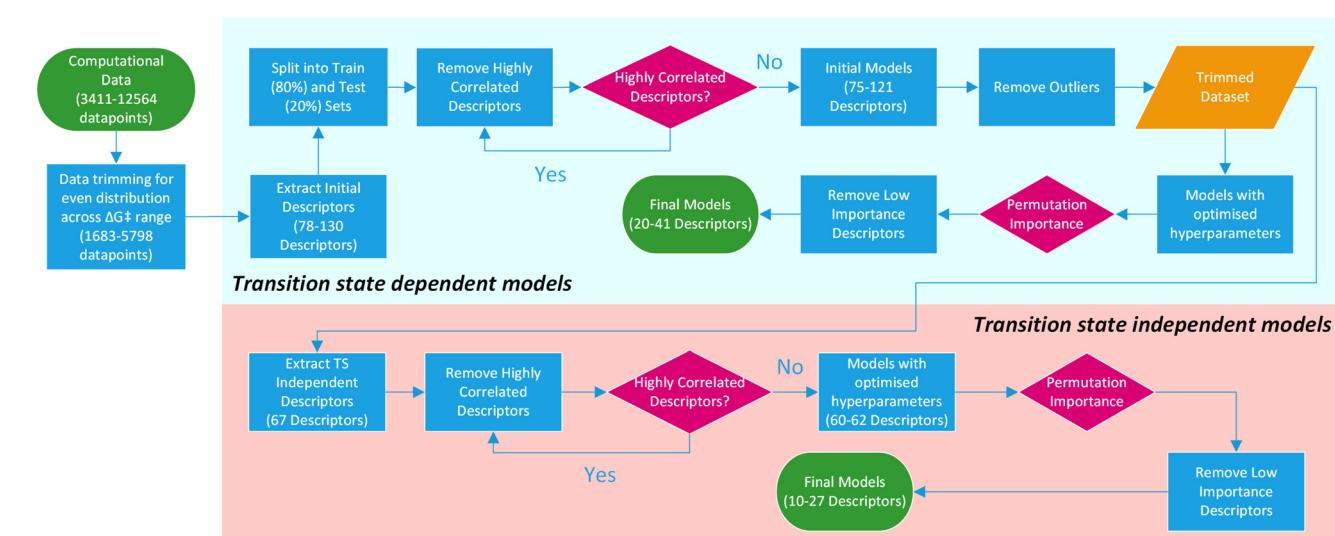
Fig. 9 Overview of the machine learning model generation process, from computational data to final models.

In order to improve the prediction models for $\Delta G^{\ddagger}$ without calculating the transition states, some of the freed-up computational time was dedicated to the calculation of more accurate electronic descriptors using a higher-level method. The electronic descriptors were recalculated using three DFT methods: TPSS, TPSSh and PBE0. These were selected for their previous successful calculation of first-row transition metals complexes (TPSS) and increasing amount of Hartree–Fock exchange for more accurate bonding description (TPSSh and PBE0).[65,66] The triple-ζ basis set def2-TZVP was used with all methods. The single-core CPU time for each energy method for 50 **IPip/IPyr** structures is 14, 34, 94 and 86 hours for B97-3c, TPSS, TPSSh and PBE0, respectively. The correlation of electronic descriptors and activation energy with those from DLNPO-CCSD(T)/def2-TZVPP were examined (see ESI,† Table S28), and PBE0 and TPSS were selected for prediction model building based on either accuracy or speed. In each case, the new $\Delta G^{\ddagger}$ values from PBE0 or TPSS replaced the values from B97-3c in these models.

Surprisingly, the TPSS-based models outperformed those based on PBE0 with better RMSE metrics across all four datasets, requiring only a third of the CPU time compared to that of PBE0. On average, the computational time per new prediction of $\Delta G^{\ddagger}$ was reduced from ~10 h, for transition state based B97-3c//GFN2-xTB models, to ~1 h using TPSS-def2-TZVP//GFN2-xTB descriptors based on **IPyr** or **IPip**. The predictions for the *PIP_TSSig_TPSS* dataset are well within the error of the calculated activation energies (3.9 kcal mol⁻¹). These are very significant improvements to the B97-3c//GFN2-xTB models both with and without the inclusion of the transition state descriptors. This new method using ML algorithms to predict $\Delta G^{\ddagger}$ provides an excellent balance between accuracy and speed for high-throughput ligand/catalyst development.

Lastly, the trend in descriptor importance is consistent between the transition state dependent and transition state independent models. The **TSOA** $\Delta G^{\ddagger}$ is dependent on the ability of the ligand to modulate the electron density at the copper centre *via* the s/d orbitals. The lack of amine nitrogen

This journal is © The Royal Society of Chemistry 2023

Catal. Sci. Technol., 2023, **13**, 2407–2420 | **2417**

Table 7 Metrics of the best-performing models for the descriptors sets without using the transition state with different descriptor sets and with descriptors and activation energies calculated at the PBE0/def2-TZVP and TPSS/def2-TZVP levels of theory

Dataset	Best algorithm	R^2	RMSE	%$\Delta G^{\ddagger} \pm 4$
Full descriptors				
PIP_set_TSOA_NoTS	SVM	0.32	6.56	79.6
PYR_set_TSOA_NoTS	SVM	0.67	5.16	68.1
PIP_set_TSSig_NoTS	SVM	0.57	3.74	83.7
PYR_set_TSSig_NoTS	ET	0.66	4.83	75.8
Trimmed descriptors				
PIP_set_TSOA_NoTS	ET	0.29	6.95	76.3
PYR_set_TSOA_NoTS	ET	0.69	4.97	66.4
PIP_set_TSSig_NoTS	SVM	0.56	3.78	82.8
PYR_set_TSSig_NoTS	ET	0.64	4.98	75.8
PBE0 electronic descriptors				
PIP_TSOA_PBE0	SVM	0.40	6.11	82.3
PYR_TSOA_PBE0	SVM	0.71	4.59	72.6
PIP_TSSig_PBE0	SVM	0.69	3.78	84.6
PYR_TSSig_PBE0	ET	0.68	4.66	78.0
TPSS electronic descriptors				
PIP_TSOA_TPSS	ET	0.34	6.03	80.5
PYR_TSOA_TPSS	SVM	0.69	4.27	75.4
PIP_TSSig_TPSS	ET	0.62	3.46	87.8
PYR_TSSig_TPSS	ET	0.70	4.09	80.4

descriptors within the top 5 most important descriptors, after which change in R^2 drops significantly, implies that the interaction between the copper and nucleophile is of low importance, which can be justified by the lack of N participation in the oxidative addition transition state. The **TSSig** $\Delta G^{\ddagger}$ is dependent on the ability of the ligand to create the correct orientation and modulate the electron density on the nucleophile nitrogen. In the case of an amide nucleophile, this is achieved through the weakening of the amide bond.

4 Conclusions

We have presented a novel semi-automated, high-throughput computational workflow for ligand/catalyst development based on the prediction of $\Delta G^{\ddagger}$ in copper(ɪ)-catalysed C–N coupling reactions and the CSD. This workflow (i) automatically generates organometallic intermediates and transition states, (ii) performs computational calculations for the determination of structural and electronic properties, and (iii) analyses and predicts the activation energy for each ligand. Importantly, ML models were developed based on the high-throughput computational output to accurately predict the activation energy barriers while bypassing the costly calculation of the transition states. These models performed very well against the "gold-standard" coupled-cluster method, with typically 75–88% of predictions $< \pm 4$ kcal mol^{-1} at a much lower computational cost. Models were analysed to

identify potentially important ligand features for the design of new catalysts.

This workflow offers significant advantages over currently used methods due to its faster speed and good to excellent accuracy compared to higher-level methods. We expect this workflow to have wide applicability in catalyst design, ranging from pharmaceutical process development to novel catalyst design across multiple chemical areas. Further development toward fully automated processes is in progress and will benefit the wider chemistry community.

Data availability

All code used in the presented work is freely available *via* Zenodo at **https://doi.org/10.5281/zenodo.7390425** with all the datasets presented in this manuscript.

Author contributions

M. A. S. S. carried out the data analysis and all the computational and machine learning work. B. N. N., C. E. W. and C. A. T. provided scientific insights and guided the direction of the project. The manuscript was written by M. A. S. S. and B. N. N.

Conflicts of interest

There are no conflicts to declare.

Acknowledgements

Notes and references

1 J. Lu, S. Donnecke, I. Paci and D. C. Leitch, *Chem. Sci.*, 2022, **13**, 3477–3488.
2 T. Gensch, G. dos Passos Gomes, P. Friederich, E. Peters, T. Gaudin, R. Pollice, K. Jorner, A. Nigam, M. Lindner-Dâ€™Addario, M. S. Sigman and A. Aspuru-Guzik, *J. Am. Chem. Soc.*, 2022, **144**, 1205–1217.
3 N. Fey, A. Koumi, A. V. Malkov, J. D. Moseley, B. N. Nguyen, S. N. G. Tyler and C. E. Willans, *Dalton Trans.*, 2020, **49**, 8169–8178.
4 D. J. Durand and N. Fey, *Chem. Rev.*, 2019, **119**, 6561–6594.
5 J. Jover, N. Fey, J. N. Harvey, G. C. Lloyd-Jones, A. G. Orpen, G. J. J. Owen-Smith, P. Murray, D. R. J. Hose, R. Osborne and M. Purdie, *Organometallics*, 2012, **31**, 5302–5306.
6 N. Fey, J. N. Harvey, G. C. Lloyd-Jones, P. Murray, A. G. Orpen, R. Osborne and M. Purdie, *Organometallics*, 2008, **27**, 1372–1383.
7 N. Fey, A. C. Tsipis, S. E. Harris, J. N. Harvey, A. G. Orpen and R. A. Mansson, *Chem. – Eur. J.*, 2006, **12**, 291–302.

2418 | *Catal. Sci. Technol.*, 2023, **13**, 2407–2420

This journal is © The Royal Society of Chemistry 2023

8 B. Cheng, H. Yi, C. He, C. Liu and A. Lei, *Organometallics*, 2015, **34**, 206–211.

9 C. Poree and F. Schoenebeck, *Acc. Chem. Res.*, 2017, **50**, 605–608.

10 G. J. Sherborne, S. Adomeit, R. Menzel, J. Rabeah, A. Brückner, M. R. Fielding, C. E. Willans and B. N. Nguyen, *Chem. Sci.*, 2017, **8**, 7203–7210.

11 J.-P. Lange, *Nat. Catal.*, 2021, **4**, 186–192.

12 K. Wu and A. G. Doyle, *Nat. Chem.*, 2017, **9**, 779–784.

13 H. J. Kulik and M. S. Sigman, *Acc. Chem. Res.*, 2021, **54**, 2335–2336.

14 Y. Amar, A. M. Schweidtmann, P. Deutsch, L. Cao and A. Lapkin, *Chem. Sci.*, 2019, **10**, 6697–6706.

15 D. T. Ahneman, J. G. Estrada, S. Lin, S. D. Dreher and A. G. Doyle, *Science*, 2018, **360**, 186–190.

16 A. F. Zahrt, J. J. Henle, B. T. Rose, Y. Wang, W. T. Darrow and S. E. Denmark, *Science*, 2019, **363**, 1–11.

17 H. Tian and S. Rangarajan, *J. Chem. Theory Comput.*, 2019, **15**, 5588–5600.

18 S. Dohm, M. Bursch, A. Hansen and S. Grimme, *J. Chem. Theory Comput.*, 2020, **16**, 2002–2012.

19 C. Bannwarth, E. Caldeweyher, S. Ehlert, A. Hansen, P. Pracht, J. Seibert, S. Spicher and S. Grimme, *WIREs Comput. Mol. Sci.*, 2021, **11**, e1493.

20 C. Bannwarth, S. Ehlert and S. Grimme, *J. Chem. Theory Comput.*, 2019, **15**, 1652–1671.

21 M. Bursch, H. Neugebauer and S. Grimme, *Angew. Chem., Int. Ed.*, 2019, **58**, 11078–11087.

22 M. H. S. Segler, M. Preuss and M. P. Waller, *Nature*, 2018, **555**, 604–610.

23 C. W. Coley, W. H. Green and K. F. Jensen, *Acc. Chem. Res.*, 2018, **51**, 1281–1289.

24 K. L. Dobo, N. Greene, C. Fred, S. Glowienke, J. S. Harvey, C. Hasselgren, R. Jolly, M. O. Kenyon, J. B. Munzner, W. Muster, R. Neft, M. Vijayaraj Reddy, A. T. White and S. Weiner, *Regul. Toxicol. Pharmacol.*, 2012, **62**, 449–455.

25 M. Foscato and V. R. Jensen, *ACS Catal.*, 2020, **10**, 2354–2377.

26 D. V. S. Green, S. Pickett, C. Luscombe, S. Senger, D. Marcus, J. Meslamani, D. Brett, A. Powell and J. Masson, *J. Comput.-Aided Mol. Des.*, 2020, **34**, 747–765.

27 Y. Chu, W. Heyndrickx, G. Occhipinti, V. R. Jensen and B. K. Alsberg, *J. Am. Chem. Soc.*, 2012, **134**, 8885–8895.

28 S. M. Mennen, C. Alhambra, C. L. Allen, M. Barberis, S. Berritt, T. A. Brandt, A. D. Campbell, J. Castañón, A. H. Cherney, M. Christensen, D. B. Damon, J. Eugenio de Diego, S. García-Cerrada, P. García-Losada, R. Haro, J. Janey, D. C. Leitch, L. Li, F. Liu, P. C. Lobben, D. W. C. MacMillan, J. Magano, E. McInturff, S. Monfette, R. J. Post, D. Schultz, B. J. Sitter, J. M. Stevens, I. I. Strambeanu, J. Twilton, K. Wang and M. A. Zajac, *Org. Process Res. Dev.*, 2019, **23**, 1213–1242.

29 G. Lefèvre, G. Franc, A. Tlili, C. Adamo, M. Taillefer, I. Ciofini and A. Jutand, *Organometallics*, 2012, **31**, 7694–7707.

30 J. W. Tye, Z. Weng, A. M. Johns, C. D. Incarvito and J. F. Hartwig, *J. Am. Chem. Soc.*, 2008, **130**, 9971–9983.

31 G. O. Jones, P. Liu, K. N. Houk and S. L. Buchwald, *J. Am. Chem. Soc.*, 2010, **132**, 6205–6213.

32 H. L. Aalten, G. van Koten, D. M. Grove, T. Kuilman, O. G. Piekstra, L. A. Hulshof and R. A. Sheldon, *Tetrahedron*, 1989, **45**, 5565–5578.

33 V. V. Litvak and U. S. M. Shein, *Zh. Org. Khim.*, 1974, **10**, 2360.

34 J. Lindley, *Tetrahedron*, 1984, **40**, 1433–1456.

35 H. Weingarten, *J. Org. Chem.*, 1964, **29**, 3624–3626.

36 C. Sambiagio, S. P. Marsden, A. J. Blacker and P. C. McGowan, *Chem. Soc. Rev.*, 2014, **43**, 3525–3550.

37 E. Sperotto, G. P. M. van Klink, G. van Koten and J. G. de Vries, *Dalton Trans.*, 2010, **39**, 10338–10351.

38 H.-Z. Yu, Y.-Y. Jiang, Y. Fu and L. Liu, *J. Am. Chem. Soc.*, 2010, **132**, 18078–18091.

39 P.-F. Larsson, A. Correa, M. Carril, P.-O. Norrby and C. Bolm, *Angew. Chem., Int. Ed.*, 2009, **48**, 5691–5693.

40 R. Giri, A. Brusoe, K. Troshin, J. Y. Wang, M. Font and J. F. Hartwig, *J. Am. Chem. Soc.*, 2018, **140**, 793–806.

41 G. J. Sherborne, S. Adomeit, R. Menzel, J. Rabeah, A. Brückner, M. R. Fielding, C. E. Willans and B. N. Nguyen, *Chem. Sci.*, 2017, **8**, 7203–7210.

42 J. Tye, Z. Weng, R. Giri and J. Hartwig, *Angew. Chem., Int. Ed.*, 2010, **49**, 2185–2189.

43 K. K. Gurjar and R. K. Sharma, *ChemCatChem*, 2017, **9**, 862–869.

44 A. Nandy and H. Kulik, *ACS Catal.*, 2020, **10**, 15033–15047.

45 F. Liu, C. Duan and H. J. Kulik, *J. Phys. Chem. Lett.*, 2020, **11**, 8067–8076.

46 C. Duan, J. P. Janet, F. Liu, A. Nandy and H. J. Kulik, *J. Chem. Theory Comput.*, 2019, **15**, 2331–2345.

47 A. Nandy, J. Zhu, J. P. Janet, C. Duan, R. B. Getman and H. J. Kulik, *ACS Catal.*, 2019, **9**, 8243–8255.

48 N. C. Institute, *Chemical Identifier Resolver*, 2020, https://cactus.nci.nih.gov/chemical/structure.

49 E. Ioannidis, T. Gani and H. Kulik, *J. Comput. Chem.*, 2016, **37**, 2106–2117.

50 A. Rappé, C. Casewit, K. Colwell, W. Goddard and W. M. Skiff, *J. Am. Chem. Soc.*, 1992, **114**, 10024–10035.

51 M. J. Frisch, G. W. Trucks, H. B. Schlegel, G. E. Scuseria, M. A. Robb, J. R. Cheeseman, G. Scalmani, V. Barone, G. A. Petersson, H. Nakatsuji, X. Li, M. Caricato, A. V. Marenich, J. Bloino, B. G. Janesko, R. Gomperts, B. Mennucci, H. P. Hratchian, J. V. Ortiz, A. F. Izmaylov, J. L. Sonnenberg, D. Williams-Young, F. Ding, F. Lipparini, F. Egidi, J. Goings, B. Peng, A. Petrone, T. Henderson, D. Ranasinghe, V. G. Zakrzewski, J. Gao, N. Rega, G. Zheng, W. Liang, M. Hada, M. Ehara, K. Toyota, R. Fukuda, J. Hasegawa, M. Ishida, T. Nakajima, Y. Honda, O. Kitao, H. Nakai, T. Vreven, K. Throssell, J. A. Montgomery, Jr., J. E. Peralta, F. Ogliaro, M. J. Bearpark, J. J. Heyd, E. N. Brothers, K. N. Kudin, V. N. Staroverov, T. A. Keith, R. Kobayashi, J. Normand, K. Raghavachari, A. P. Rendell, J. C. Burant, S. S. Iyengar, J. Tomasi, M. Cossi, J. M. Millam, M. Klene, C. Adamo, R. Cammi, J. W. Ochterski, R. L. Martin, K. Morokuma, O. Farkas, J. B. Foresman and D. J. Fox, *Gaussian 09 Revision D.01*, Gaussian Inc., Wallingford CT, 2009.

This journal is © The Royal Society of Chemistry 2023

Catal. Sci. Technol., 2023, **13**, 2407–2420 | **2419**

52 F. Neese, *WIREs Comput. Mol. Sci.*, 2018, **8**, e1327.

53 C. Riplinger, B. Sandhoefer, A. Hansen and F. Neese, *J. Chem. Phys.*, 2013, **139**, 134101.

54 A. V. Marenich, C. J. Cramer and D. G. Truhlar, *J. Phys. Chem. B*, 2009, **113**, 6378–6396.

55 A. Onufriev, D. Bashford and D. A. Case, *Proteins: Struct., Funct., Bioinf.*, 2004, **55**, 383–394.

56 GitHub - kjelljorner/morfeus: A Python package for calculating molecular features — github.com, **https://github.com/kjelljorner/morfeus#readme**, [Accessed 31-May-2022].

57 T. Akiba, S. Sano, T. Yanase, T. Ohta and M. Koyama, *Proceedings of the 25rd ACM SIGKDD International Conference on Knowledge Discovery and Data Mining*, 2019.

58 W. Kabsch, *Acta Crystallogr., Sect. A: Cryst. Phys., Diffr., Theor. Gen. Crystallogr.*, 1976, **32**, 922–923.

59 O. Korb, B. Kuhn, J. Hert, N. Taylor, J. Cole, C. Groom and M. Stahl, *J. Med. Chem.*, 2016, **59**, 4257–4266.

60 J. G. Brandenburg, C. Bannwarth, A. Hansen and S. Grimme, *J. Chem. Phys.*, 2018, **148**, 064104.

61 L. D. Jacobson, A. D. Bochevarov, M. A. Watson, T. F. Hughes, D. Rinaldo, S. Ehrlich, T. B. Steinbrecher, S. Vaitheeswaran, D. M. Philipp, M. D. Halls and R. A. Friesner, *J. Chem. Theory Comput.*, 2017, **13**, 5780–5797.

62 P. Vermeeren, X. Sun and F. M. Bickelhaupt, *Sci. Rep.*, 2018, **8**, 10729.

63 W.-J. van Zeist, R. Visser and F. Bickelhaupt, *Chem. – Eur. J.*, 2009, **15**, 6112–6115.

64 L. Breiman, *Mach. Learn.*, 2001, **45**, 5–32.

65 M. Bühl and H. Kabrede, *J. Chem. Theory Comput.*, 2006, **2**, 1282–1290.

66 M. P. Waller, H. Braun, N. Hojdis and M. Bühl, *J. Chem. Theory Comput.*, 2007, **3**, 2234–2242.

2420 | *Catal. Sci. Technol.*, 2023, **13**, 2407–2420

This journal is © The Royal Society of Chemistry 2023